

Topological superconductor candidates PdBi_2Te_4 and PdBi_2Te_5 from a generic ab initio strategy

Aiyun Luo,^{1,*} Ying Li,^{1,*} Yi Qin,^{1,*} Jingnan Hu,¹ Biao Lian,² and Gang Xu^{1,3,4,†}

¹Wuhan National High Magnetic Field Center & School of Physics,
Huazhong University of Science and Technology, Wuhan 430074, China

²Department of Physics, Princeton University, Princeton, NJ 08544, United States of America

³Institute for Quantum Science and Engineering,
Huazhong University of Science and Technology, Wuhan 430074, China

⁴Wuhan Institute of Quantum Technology, Wuhan 430074, China

Superconducting topological metals (SCTMs) have recently emerged as a promising platform of topological superconductivity (TSC) and Majorana zero modes (MZMs) for quantum computation. Despite their importance in both fundamental research and applications, SCTMs are very rare in nature. In addition, some superconductors with topological electronic structures have been reported recently, but a feasible program to determine their TSC properties is still lacking. Here, we propose a new strategy to design SCTMs by intercalating the superconducting units into the topological insulators. A program that characterizes the superconducting BdG Chern number of 2D BdG Hamiltonian from ab initio calculations is also developed. Following this strategy, PdBi_2Te_5 and PdBi_2Te_4 are found to be experimentally synthesizable and ideal SCTMs. Chiral TSC could be realized in such SCTMs by incorporating topological surface states with Zeeman effect, which can be realized by an external magnetic field or in proximity to ferromagnetic (FM) insulator. Our strategy provides a new method for identifying the SCTMs and TSC candidates, and the program makes it possible to design and modulate the TSC candidates from ab initio calculations.

MAIN

As one of the most important systems in both fundamental physics and topological quantum computation, topological superconductors (TSCs) have attracted increasing interest for their ability to support Majorana fermions and anyons with non-Abelian statistics [1–17]. Currently, the search for TSCs candidates has been focused on two

* These authors made equal contributions to this work.

† e-mail address: gangxu@hust.edu.cn

experimental schemes. One is the architectures by the combination of conventional superconductors with topological insulators (TIs) [18–20] or 1D nanowires [21, 22], but this approach brings high requirements for sample fabrication and interface engineering. The other route is to achieve TSCs in superconducting topological metals (SCTMs) that host both topological electronic structures at the Fermi level and superconductivity in one compound [23–36], in which the topological surface states are gapped by the “self-proximity effect” of bulk superconductivity, thus avoiding the complications of interface engineering. This approach has successfully predicted the SCTM $\text{FeTe}_{0.55}\text{Se}_{0.45}$ [24–26] and similar compounds of iron-based superconductors [27–30], owing to the favorable SC gap and non-trivial band topology. Beside the MZMs, 1D helical/chiral Majorana states have also been reported in domain walls of $\text{FeTe}_{0.55}\text{Se}_{0.45}$ [37] and the magnetism-superconductor heterostructures [38–45]. It is also proposed that the propagating chiral Majorana states can be applied to realize non-Abelian quantum gate operations, which could be 10^3 faster than the currently existing quantum computation schemes [46].

Encouraged by the success of $\text{Fe}(\text{Se},\text{Te})$ [24–26], many topological materials that host both superconductivity and topological electronic structures are proposed [47–52]. However, very rare experimental progress of TSC has been made in such SCTMs. This is because, on the one hand, all of them are not the ideal SCTMs, whose band structures are too complicated, the topological surface states are usually buried in the bulk states and difficult to form the pairing required by TSC. On the other hand, lacking a direct characterization of the TSC properties from ab initio calculations also hinders the effective experimental search in such materials. Therefore, a general program that could calculate the TSC invariant from first-principles calculations is highly desirable.

In this work, we develop a program to characterize the superconducting topological invariant of 2D system from ab initio calculations. Besides, we also propose a new strategy to design ideal SCTMs by intercalating superconducting units into topological insulators. Following this strategy, PdBi_2Te_5 and PdBi_2Te_4 are found to be ideal SCTMs that host topological surface states at the Fermi level and superconductivity at 0.57 K and 3.11 K respectively. By performing the superconducting energy spectrum and topological invariant calculations, we identify that chiral TSC could be realized in the slab of such SCTMs by introducing considerable Zeeman splitting on the topological surface states, which can be realized by an external magnetic field or in proximity to FM insulators. Our strategy provides a new framework to enrich SCTMs and TSC candidates, and the program makes it possible to design and modulate the TSC system from ab initio calculations, which can also be extended to study the TSC properties in other system, such as magnetic TI/SC heterostructure, SC/FM heterostructure and SC/TI/SC heterostructure.

Inspired by the construction of magnetic TI MnBi_2Te_4 [53, 54], we propose that the SCTMs can be designed by

intercalating the SC units into the TIs, as illustrated by the schematic of Fig. 1(a). As an ideal SCTM, the target crystal should be relatively stable in both energy and structure. More importantly, it must inherit the topological electronic structures of the parent TI near the Fermi level, and also the superconductivity of the parent SC as shown in Fig. 1(b). However, the combination of topological electronic structures and SC does not result in TSC eventually. The realization of TSC generally requires a delicate modulation of many parameters, such as SC pairing, Zeeman splitting and chemical potential, et al [18–26, 38–45]. Thus, the ability to characterize the TSC invariant and determine the required parameters in real materials from the ab initio calculations is not only of theoretical significance, but also highly desirable in experiment.

Here we develop a program to simulate the superconducting properties and characterize its topological invariant in 2D slab system from ab initio calculations, in which the necessary ingredients to realize chiral TSC based on SCTM are included, such as bulk band structures, SC pairing, Zeeman splitting, Rashba spin-orbit coupling and chemical potential. The workflow of this program is shown in Fig. 2. First, one should calculate the electronic structures of SCTM materials, and construct the localized Wannier functions that capture all electronic features from the first-principles calculations, referred as \hat{H}_{bulk} . The next step is to construct the slab Hamiltonian \hat{H}_{slab} with open boundary condition along a certain direction [55]. In general, the spin-orbit coupling (SOC) and surface effect can be included automatically in \hat{H}_{slab} through the first-principles calculations with SOC. So that the topological properties, such as the surface states and spin-texture, can be directly studied by using \hat{H}_{slab} . On the other hand, one can also construct a slab Hamiltonian $\hat{H}_{\text{slab}}^{\text{nsoc}}$ that excluded SOC from the non-SOC first-principles calculations, and add \hat{H}_{SOC} and \hat{H}_{surf} manually to simulate the variable SOC and surface effect in the topological electronic states and TSC. In this work, we will adopt the former type of \hat{H}_{slab} , in which only the intrinsic SOC of the real material is included. With adopting particle-hole transformation, the \hat{H}_{slab} can be extended to BdG Hamiltonian $\hat{H}_{\text{slab}}^{\text{BdG}}$ by adding SC pairing \hat{H}_{sc} and Zeeman splitting \hat{H}_{z} . In the Nambu basis $\Phi_{\mathbf{k}} = (c_{\mathbf{k},j,\alpha,\uparrow}, c_{\mathbf{k},j,\alpha,\downarrow}, c_{-\mathbf{k},j,\alpha,\uparrow}^\dagger, c_{-\mathbf{k},j,\alpha,\downarrow}^\dagger)$, where the $c_{j,\alpha,\sigma}$ is the fermion operator denotes an electron at j layer with orbital α and spin $\sigma(\uparrow, \downarrow)$, the BdG Hamiltonian is formulated as:

$$H_{\text{slab}}^{\text{BdG}}(\mathbf{k}) = \begin{pmatrix} H_{\text{slab}}(\mathbf{k}) - \mu & \Delta(\mathbf{k}) \\ \Delta^\dagger(\mathbf{k}) & -H_{\text{slab}}^*(-\mathbf{k}) + \mu \end{pmatrix} + M_z \tau_z. \quad (1)$$

In Eq. 1, μ is the chemical potential, which can be used to simulate the carriers doping. $\Delta(\mathbf{k})$ denotes the SC pairing matrices, which could be both singlet and triplet pairing form. For the conventional s -wave SC, $\Delta(\mathbf{k})$ is expressed as:

$$\Delta(\mathbf{k}) = \Delta_s \times I_{\text{slab}} \otimes (i\sigma_y \otimes I_{\text{orb}}), \quad (2)$$

where Δ_s is the magnitude of intrinsic bulk s -wave pairing, σ_y is the Pauli matrix in spin space, I_{slab} (I_{orb}) is an $\mathcal{N}_{slab} \times \mathcal{N}_{slab}$ ($\mathcal{N}_{orb} \times \mathcal{N}_{orb}$) identity matrix that represents the number of slab layers (Wannier orbitals). τ_z is the Pauli matrix in particle-hole space, M_z is the Zeeman splitting energy, and $H_z = M_z \tau_z$ is used to simulate the influence of the external magnetic field or the proximity effect of the FM insulator. Thus, H_z can be chosen to be applied for the whole slab or just few surface layers, depending on the slab thickness, strength of magnetic field, the type of the SC et al. In principle, chiral TSC can be achieved by modulating the SC pairing, Zeeman splitting and chemical potential [38–45], which can be further revealed by calculating the superconducting energy spectrum and the superconducting topological invariant.

In the gaped 2D superconducting system, the topological superconductors are classified by BdG Chern number in the absence of time-reversal symmetry [3]. Such superconducting topological invariants can be characterized by the evolution of Wilson loop [56–58]. For the occupied quasiparticle states $|u_{n,k_1,k_2}^{\text{BdG}}\rangle$, where k_1 and k_2 are momenta along two primitive vectors of the Brillouin zone (BZ), the Berry phase of the Wilson loop along k_2 at a fixed k_1 can be expressed as:

$$\mathcal{W}(k_1) = -\text{Im} \ln \prod_i \det M_{k_1}^{(i)}, \quad (3)$$

with the overlap matrix $M_{k_1,mn}^{(i)} = \langle u_{m,k_1,k_2}^{\text{BdG}} | u_{n,k_1,k_2}^{\text{BdG}} \rangle$, where $k_2^{(i)}$ is the i -th discretized momenta along k_2 direction. The winding number of $\mathcal{W}(k_1)$ with respect to k_1 is equal to the superconducting BdG Chern number C_{BdG} .

Next, we take TI Bi_2Te_3 [59, 60], SC PdTe [61, 62] and SC PdTe_2 [50–52] as parent compounds to demonstrate that our SCTMs strategy is feasible. Experimentally, Bi_2Te_3 (space group $R\bar{3}m$, $a = 4.35 \text{ \AA}$, $c = 30.36 \text{ \AA}$), PdTe (space group $P6_3/mmc$, $a = 4.152 \text{ \AA}$, $c = 5.671 \text{ \AA}$, $T_c = 2.3 \text{ K}$) and PdTe_2 (space group $P\bar{3}m1$, $a = 4.03 \text{ \AA}$, $c = 5.12 \text{ \AA}$, $T_c = 1.64 \text{ K}$) all adopt the triangle lattice and have very similar in-plane lattice constants, which makes it much easier to integrate them together to form a new compound. According to our calculations, the stable unit of PdBi_2Te_5 and PdBi_2Te_4 adopt octuple-layer (OL) structure and septuple-layer (SL) structure respectively, as shown in Fig. 3(a)(also Fig. S1) and Fig. S2 of Supplementary Material(SM) [63]. They both favor the ABC stacking along c -direction, and form the rhombohedral unit cell as shown in Fig. 3(a), which is 73 meV/f.u. (73 meV/f.u. for PdBi_2Te_4) and 46 meV/f.u. (12 meV/f.u. PdBi_2Te_4) lower than the AA and AB stacking structures. The detailed crystal parameters and total energy of different stacking PbBi_2Te_5 and PbBi_2Te_4 are tabulated in the Table. S1 and Table. S2, respectively [63].

The formation energy of PdBi_2Te_5 and PdBi_2Te_4 are calculated to study their thermodynamic stability by using $E_f^{\text{Pd}_m\text{Bi}_n\text{Te}_l} = E^{\text{Pd}_m\text{Bi}_n\text{Te}_l} - mE^{\text{Pd}} - nE^{\text{Bi}} - lE^{\text{Te}}$, with E^i ($i=\text{Pd}_m\text{Bi}_n\text{Te}_l, \text{Pd}, \text{Bi}$ and Te) means the calculated

total energy per formula in the ground state. The calculated $E_f^{PdBi_2Te_5}$ and $E_f^{PdBi_2Te_4}$ are -3.184 eV/f.u. and -2.476 eV/f.u., which means that 3.184 eV and 2.476 eV can be released during their synthesis processes from the constituent elements. To further manifest their thermodynamic stability, we construct the convex hull diagram in Fig. 3(b) with all of the synthesized Pd-Bi-Te compounds, whose crystal parameters and the calculated formation energy have been tabulated in Table. S3 and Table. S4, respectively [63]. Fig. 3(b) shows that $PdBi_2Te_5$ and $PdBi_2Te_4$ are 13 meV/atom and 61 meV/atom above the convex hull respectively. Moreover, considering that metastable $PdBi_2Te_3$, 52 meV and 3 meV higher than $PdBi_2Te_5$ and $PdBi_2Te_4$ as shown in Fig. 3(b), has been synthesized in experiments [64, 65], we thus conclude that $PdBi_2Te_5$ and $PdBi_2Te_4$ could be synthesized in experiments. For $PdBi_2Te_5$, we propose a synthetic route through the growth of Bi_2Te_3 and $PdTe_2$ layer by layer. Our calculated results reveal that bulk $PdBi_2Te_5$ is 59 meV/f.u. lower than the total energy of free standing Bi_2Te_3 and $PdTe_2$ layers, which strongly suggest that $PdTe_2$ layer tends to deposit on Bi_2Te_3 to form new $PdBi_2Te_5$ crystal. To investigate their dynamical stability, we calculate the phonon dispersion of $PdBi_2Te_5$ and $PdBi_2Te_4$, and plot them in Fig. 3(c) and Fig. S3(a) [63]. There are 24 (21) phonon modes with fully real positive frequencies for $PdBi_2Te_5$ ($PdBi_2Te_4$), which indicates that the rhombohedral unit cells are dynamically stable. Based on these results, we conclude that $PdBi_2Te_5$ and $PdBi_2Te_4$ are relatively thermodynamically and dynamically stability in the rhombohedral structure, and further experimental investigation is called for.

Then we study the electronic structures and topological properties of $PdBi_2Te_5$ and $PdBi_2Te_4$. Since $PdBi_2Te_5$ and $PdBi_2Te_4$ exhibit similar electronic structures and non-trivial band topology, we only show the detailed density of states (DOS), band structures, and topological surface states of $PdBi_2Te_5$ as an example in the main text, one can check the results of $PdBi_2Te_4$ in Section III and Figs. S3 of the SM [63]. In Fig. 3(d), we plot the total and projected DOS of $PdBi_2Te_5$, which gives rise to $DOS(0 \text{ eV}) = 1.91$ states/eV at Fermi level, indicating its metallic nature and the possibility of superconductivity. The projected DOS demonstrates that the states between -1 eV and 1 eV are dominated by the p -orbitals of Te hybridized with d -orbitals from Pd and p -orbitals from Bi. The hybridization is also manifested by the projected band structures shown in Fig. 3(e), which shows that two bands with p -orbital components from Te or Bi cross the Fermi level and form several Fermi surfaces. Further detailed orbital components analysis demonstrates that a continuous band gap (yellow region in Fig. 3(e)) and band inversion exists between the nominal valence band and conduction band around the Fermi level, which implies that $PdBi_2Te_5$ inherits the topological electronic nature of Bi_2Te_3 successfully. The nontrivial band topology can be confirmed by calculating the Z_2 topological invariant of time-reversal invariant insulators [66]. Given that rhombohedral $PdBi_2Te_5$

possesses inversion symmetry and a continuous band gap, the Z_2 topological invariant $\nu_{\text{TI}} = (1 - P)/2$ is determined by the product P of the parity of the wave function at the TRIM points [66]. Our calculated results give Z_2 index $\nu_{\text{TI}} = 1$, confirming PdBi_2Te_5 is a Z_2 topological metal. To visualize the bulk–boundary correspondence, we calculate and plot the topological surface states on the (001) surface in Fig. 3(f). The surface states are similar to that of Bi_2Te_3 [59, 60], the Dirac cone at the Γ point manifest approximately -6.3 meV below the Fermi level (the dashed line in Fig. 3(f)).

To investigate the superconducting property of PdBi_2Te_5 , we perform the electron-phonon calculations based on density functional perturbation theory [67]. The calculated electron-phonon coupling constant $\lambda = 0.43$ and logarithmic average phonon frequency $\omega_{\text{log}} = 97 \text{ cm}^{-1}$, as tabulated in Table. S5 [63]. Furthermore, the superconducting transition temperature (T_c) is estimated by using the reduced Allen-Dynes formula [68, 69]:

$$T_c = \frac{\omega_{\text{log}}}{1.20} \exp \left[-\frac{1.04(1 + \lambda)}{\lambda - \mu^*(1 + 0.62\lambda)} \right], \quad (4)$$

where μ^* is the effective Coulomb potential. By adopting a typical $\mu^* = 0.1$, the T_c of PdBi_2Te_5 is estimated as 0.57 K. As comparison, the calculated λ and ω_{log} in PdTe_2 is 0.52 and 112 cm^{-1} , respectively. Accordingly, the estimated T_c in PdTe_2 is 1.59 K, which agrees well with the experimental T_c of 1.64 K [50–52]. These results clearly demonstrate that the SC in PdTe_2 is well inherited into the PdBi_2Te_5 .

We now study the TSC property of the PdBi_2Te_5 slab by introducing the SC pairing and Zeeman splitting into the topological surface states. Usually, the Zeeman splitting is applied by external magnetic field or in proximity to a FM insulator, as illustrated in Fig. 4(a). As a concrete example, we use a 2D slab consisting of 10-OL PdBi_2Te_5 , which is thick enough to avoid the hybridization between top layer and bottom layer (Fig. 3(f)). Since PdBi_2Te_5 is an intrinsic SC, the estimated s -wave superconducting gap $\Delta_s = 1.0$ meV is introduced globally for all 10-OLs. The out-of-plane Zeeman splitting is applied only in the bottom layer consisting of one Bi_2Te_3 and one PdTe_2 , by assuming PdBi_2Te_5 is the conventional SC from the parent type-I SC PdTe_2 [50]. The chemical potential μ is set at the energy of surface Dirac cone at the Γ point (about -6.3 meV below the Fermi level). In Fig. 4(b), we show the low energy spectrum of H_{BdG} at Γ point as a function of Zeeman splitting energy M_z , which manifest that the superconducting spectrum is fully gaped with an energy gap of Δ at $M_z = 0$. As M_z increases, the superconducting gap at the Γ point closes and reopens. This behavior indicates that a topological phase transition happens at critical point $M_z/\Delta = 3.1$, and this 2D slab enters chiral TSC phase characterized by a nonzero BdG Chern number and chiral Majorana edge states according to previous model simulations [38–40].

To firmly verify its topological property and visualize the low energy physics in the TSC phase, we calculate the

superconducting energy spectrum at $M_z=5$ meV and $\Delta=1$ meV in Fig. 4(c). The corresponding Wilson loop evolutions for the occupied states are plotted in Fig. 4(d). The zoom-in image of Fig. 4(c) reveals that a full superconducting gap is opened in the whole BZ, indicating that the system is a well defined chiral TSC. The Wilson loop evolution exhibits a nontrivial chiral winding number 1, which directly confirms the superconducting BdG Chern number $C_{\text{BdG}} = 1$. Given that the experimental accessible magnetization energy usually reaches a few tens of meV, our results provide a feasible guideline for discovery the chiral TSC phase in PdBi_2Te_5 .

Finally, we would like to point out that the chiral TSC phase could also be realized in PdBi_2Te_4 as shown in Fig. S4 [63], which exhibits a similar superconducting spectrum gap closing behavior with respect to M_z/Δ as in PdBi_2Te_5 . In addition, we emphasize that our material design strategy can also be applied to search for other SCTM candidates. For example, our calculated results demonstrate that AuBi_2Te_5 formed by SC AuTe_2 interacting into Bi_2Te_3 is also an ideal SCTM, whose detailed crystal structures, dynamic stability, electronic structures, and topological surface states are discussed in Section V and Fig. S5 of SM [63]. Therefore, we expect that SCTM AuBi_2Te_5 could also be a TSC candidate. Last, we would like to point out that the program can be extended to study many 2D topological superconducting heterostructure systems, such as magnetic TI/SC heterostructure, SC/FM heterostructure and SC/TI/SC heterostructure. This will make it possible to determine the accurate parameters of the TSC phase and simulate their TSC property in such systems from first-principles calculations. We expect our program to be also useful for optimizing the experimental setup, stimulating the field of TSC study.

ACKNOWLEDGMENTS

This work is supported by the National Key Research and Development Program of China (2018YFA0307000), and the National Natural Science Foundation of China (12274154, 11874022). B.L. is supported by the Alfred P. Sloan Foundation, the National Science Foundation through Princeton University's Materials Research Science and Engineering Center DMR-2011750, and the National Science Foundation under award DMR-2141966.

METHOD

The first-principles calculations based on density functional theory are performed by the Vienna ab initio simulation package [70, 71] with treating Perdew–Burke–Ernzerhof type of generalized gradient approximation as the exchange-correlation potential [72]. The cutoff energy for wave function expansion is set as 450 eV, k -points grid $13 \times 13 \times 13$

is used for sampling the first BZ. All crystal structures are fully optimized until the force on each atom is less than $0.01 \text{ eV}/\text{\AA}$, and the SOC is included self-consistently. The electron-phonon coupling calculations with van der Waals correction [73] are carried out in Quantum Espresso [74] based on the perturbation theory. A Hermite-Gaussian smearing of 0.0025 Ryd is used for the electronic integration. The $8 \times 8 \times 8$ k -mesh is used for the electron-phonon coupling strength λ calculations, and the dynamical matrices are calculated on a $4 \times 4 \times 4$ phonon-momentum grid. Besides, a $2 \times 2 \times 2$ supercell is built to calculate the phonon dispersion by using PHONOPY [75]. For the surface calculation, the Wannier functions of Pd- d , Bi- p and Te- p orbitals are constructed by using WANNIER90 [76]. A slab consisting of 10-OL PdBi_2Te_5 layers with a bottom surface terminated as the Bi_2Te_3 layer is implemented in WannierTools [55], which is further used to calculate the electronic surface states, the superconducting spectrum, and the superconducting BdG Chern number.

-
- [1] Nayak, C., Simon, S. H., Stern, A., Freedman, M. & Das Sarma, S. Non-abelian anyons and topological quantum computation. *Rev. Mod. Phys.* **80**, 1083–1159 (2008).
- [2] Sarma, S. D., Freedman, M. & Nayak, C. Majorana zero modes and topological quantum computation. *npj Quantum Information* **1**, 1–13 (2015).
- [3] Sato, M. & Ando, Y. Topological superconductors: a review. *Reports on Progress in Physics* **80**, 076501 (2017).
- [4] Lutchyn, R. M. *et al.* Majorana zero modes in superconductor–semiconductor heterostructures. *Nat. Rev. Mater.* **3**, 52–68 (2018).
- [5] Liu, C.-X. & Trauzettel, B. Helical Dirac-Majorana interferometer in a superconductor/topological insulator sandwich structure. *Phys. Rev. B* **83**, 220510 (2011).
- [6] Zhang, F., Kane, C. L. & Mele, E. J. Time-reversal-invariant topological superconductivity and Majorana Kramers pairs. *Phys. Rev. Lett.* **111**, 056402 (2013).
- [7] Yang, S. A., Pan, H. & Zhang, F. Dirac and Weyl superconductors in three dimensions. *Phys. Rev. Lett.* **113**, 046401 (2014).
- [8] Wang, Q.-Z. & Liu, C.-X. Topological nonsymmorphic crystalline superconductors. *Phys. Rev. B* **93**, 020505 (2016).
- [9] Wang, Q., Liu, C.-C., Lu, Y.-M. & Zhang, F. High-temperature Majorana corner states. *Phys. Rev. Lett.* **121**, 186801 (2018).
- [10] Hao, N. & Hu, J. Topological quantum states of matter in iron-based superconductors: from concept to material realization. *National Science Review* **6**, 213–226 (2019).

- [11] Zhang, R.-X., Cole, W. S. & Das Sarma, S. Helical hinge Majorana modes in iron-based superconductors. *Phys. Rev. Lett.* **122**, 187001 (2019).
- [12] Zhang, R.-X., Cole, W. S., Wu, X. & Das Sarma, S. Higher-order topology and nodal topological superconductivity in Fe(Se,Te) heterostructures. *Phys. Rev. Lett.* **123**, 167001 (2019).
- [13] Zhang, R.-X. & Das Sarma, S. Intrinsic time-reversal-invariant topological superconductivity in thin films of iron-based superconductors. *Phys. Rev. Lett.* **126**, 137001 (2021).
- [14] Wu, X. *et al.* Boundary-obstructed topological high- T_c superconductivity in iron pnictides. *Phys. Rev. X* **10**, 041014 (2020).
- [15] Giwa, R. & Hosur, P. Fermi arc criterion for surface Majorana modes in superconducting time-reversal symmetric Weyl semimetals. *Phys. Rev. Lett.* **127**, 187002 (2021).
- [16] Nayak, A. K. *et al.* Evidence of topological boundary modes with topological nodal-point superconductivity. *Nature Physics* **17**, 1413–1419 (2021).
- [17] Margalit, G., Yan, B., Franz, M. & Oreg, Y. Chiral Majorana modes via proximity to a twisted cuprate bilayer. *Phys. Rev. B* **106**, 205424 (2022).
- [18] Fu, L. & Kane, C. L. Superconducting proximity effect and Majorana fermions at the surface of a topological insulator. *Phys. Rev. Lett.* **100**, 096407 (2008).
- [19] Xu, J.-P. *et al.* Experimental detection of a Majorana mode in the core of a magnetic vortex inside a topological insulator-superconductor Bi₂Te₃/NbSe₂ heterostructure. *Phys. Rev. Lett.* **114**, 017001 (2015).
- [20] Sun, H.-H. *et al.* Majorana zero mode detected with spin selective andreev reflection in the vortex of a topological superconductor. *Phys. Rev. Lett.* **116**, 257003 (2016).
- [21] Mourik, V. *et al.* Signatures of Majorana fermions in hybrid superconductor-semiconductor nanowire devices. *Science* **336**, 1003–1007 (2012).
- [22] Nadj-Perge, S. *et al.* Observation of Majorana fermions in ferromagnetic atomic chains on a superconductor. *Science* **346**, 602–607 (2014).
- [23] Hosur, P., Ghaemi, P., Mong, R. S. K. & Vishwanath, A. Majorana modes at the ends of superconductor vortices in doped topological insulators. *Phys. Rev. Lett.* **107**, 097001 (2011).
- [24] Xu, G., Lian, B., Tang, P., Qi, X.-L. & Zhang, S.-C. Topological superconductivity on the surface of Fe-based superconductors. *Phys. Rev. Lett.* **117**, 047001 (2016).
- [25] Zhang, P. *et al.* Observation of topological superconductivity on the surface of an iron-based superconductor. *Science* **360**, 182–186 (2018).
- [26] Wang, D. *et al.* Evidence for Majorana bound states in an iron-based superconductor. *Science* **362**, 333–335 (2018).

- [27] Liu, Q. *et al.* Robust and clean Majorana zero mode in the vortex core of high-temperature superconductor (Li_{0.84}Fe_{0.16})OHFeSe. *Physical Review X* **8**, 041056 (2018).
- [28] Liu, W. *et al.* A new majorana platform in an Fe-As bilayer superconductor. *Nature Communications* **11**, 1–7 (2020).
- [29] Kong, L. *et al.* Majorana zero modes in impurity-assisted vortex of LiFeAs superconductor. *Nature Communications* **12**, 1–11 (2021).
- [30] Li, M. *et al.* Ordered and tunable Majorana-zero-mode lattice in naturally strained LiFeAs. *Nature* 1–6 (2022).
- [31] Yuan, Y. *et al.* Evidence of anisotropic Majorana bound states in 2M-WS₂. *Nature Physics* **15**, 1046–1051 (2019).
- [32] Fang, Y. *et al.* Discovery of superconductivity in 2M WS₂ with possible topological surface states. *Advanced Materials* **31**, 1901942 (2019).
- [33] Li, Y. *et al.* Observation of topological superconductivity in a stoichiometric transition metal dichalcogenide 2M-WS₂. *Nature communications* **12**, 1–7 (2021).
- [34] Lv, Y.-F. *et al.* Experimental signature of topological superconductivity and Majorana zero modes on β -Bi₂Pd thin films. *Science bulletin* **62**, 852–856 (2017).
- [35] Guan, J.-Y. *et al.* Experimental evidence of anomalously large superconducting gap on topological surface state of β -Bi₂Pd film. *Science Bulletin* **64**, 1215–1221 (2019).
- [36] Li, Y., Xu, X., Lee, M.-H., Chu, M.-W. & Chien, C. Observation of half-quantum flux in the unconventional superconductor β -Bi₂Pd. *Science* **366**, 238–241 (2019).
- [37] Wang, Z. *et al.* Evidence for dispersing 1D Majorana channels in an iron-based superconductor. *Science* **367**, 104–108 (2020).
- [38] Qi, X.-L., Hughes, T. L. & Zhang, S.-C. Chiral topological superconductor from the quantum Hall state. *Phys. Rev. B* **82**, 184516 (2010).
- [39] Wang, J., Zhou, Q., Lian, B. & Zhang, S.-C. Chiral topological superconductor and half-integer conductance plateau from quantum anomalous Hall plateau transition. *Phys. Rev. B* **92**, 064520 (2015).
- [40] He, J. J., Liang, T., Tanaka, Y. & Nagaosa, N. Platform of chiral Majorana edge modes and its quantum transport phenomena. *Communications Physics* **2**, 1–7 (2019).
- [41] Zhang, X. & Liu, F. Prediction of Majorana edge states from magnetized topological surface states. *Phys. Rev. B* **103**, 024405 (2021).
- [42] Zhang, X. *et al.* Prediction of intrinsic topological superconductivity in Mn-doped GeTe monolayer from first-principles. *npj Computational Materials* **7**, 1–8 (2021).
- [43] Ménard, G. C. *et al.* Two-dimensional topological superconductivity in Pb/Co/Si(111). *Nature Communications* **8**, 1–7 (2017).

- [44] Palacio-Morales, A. *et al.* Atomic-scale interface engineering of Majorana edge modes in a 2D magnet-superconductor hybrid system. *Science Advances* **5**, eaav6600 (2019).
- [45] Kezilebieke, S. *et al.* Topological superconductivity in a van der Waals heterostructure. *Nature* **588**, 424–428 (2020).
- [46] Lian, B., Sun, X.-Q., Vaezi, A., Qi, X.-L. & Zhang, S.-C. Topological quantum computation based on chiral Majorana fermions. *Proceedings of the National Academy of Sciences* **115**, 10938–10942 (2018).
- [47] Huang, K. *et al.* Observation of topological Dirac fermions and surface states in superconducting BaSn₃. *Phys. Rev. B* **103**, 155148 (2021).
- [48] Chen, C. *et al.* Observation of topological electronic structure in quasi-1D superconductor TaSe₃. *Matter* **3**, 2055–2065 (2020).
- [49] Ortiz, B. R. *et al.* CsV₃Sb₅: A \mathbb{Z}_2 topological kagome metal with a superconducting ground state. *Phys. Rev. Lett.* **125**, 247002 (2020).
- [50] Leng, H., Paulsen, C., Huang, Y. K. & de Visser, A. Type-I superconductivity in the Dirac semimetal PdTe₂. *Phys. Rev. B* **96**, 220506 (2017).
- [51] Das, S. *et al.* Conventional superconductivity in the type-II Dirac semimetal PdTe₂. *Phys. Rev. B* **97**, 014523 (2018).
- [52] Kudo, K., Ishii, H. & Nohara, M. Composition-induced structural instability and strong-coupling superconductivity in Au_{1-x}Pd_xTe₂. *Phys. Rev. B* **93**, 140505 (2016).
- [53] Lee, D. S. *et al.* Crystal structure, properties and nanostructuring of a new layered chalcogenide semiconductor, Bi₂MnTe₄. *CrystEngComm* **15**, 5532–5538 (2013).
- [54] Zhang, D. *et al.* Topological axion states in the magnetic insulator MnBi₂Te₄ with the quantized magnetoelectric effect. *Phys. Rev. Lett.* **122**, 206401 (2019).
- [55] Wu, Q., Zhang, S., Song, H.-F., Troyer, M. & Soluyanov, A. A. Wanniertools: An open-source software package for novel topological materials. *Computer Physics Communications* **224**, 405–416 (2018).
- [56] Yu, R., Qi, X. L., Bernevig, A., Fang, Z. & Dai, X. Equivalent expression of \mathbb{Z}_2 topological invariant for band insulators using the non-abelian berry connection. *Phys. Rev. B* **84**, 075119 (2011).
- [57] Soluyanov, A. A. & Vanderbilt, D. Computing topological invariants without inversion symmetry. *Phys. Rev. B* **83**, 235401 (2011).
- [58] Gresch, D. *et al.* Z₂pack: Numerical implementation of hybrid wannier centers for identifying topological materials. *Phys. Rev. B* **95**, 075146 (2017).
- [59] Zhang, H. *et al.* Topological insulators in Bi₂Se₃, Bi₂Te₃ and Sb₂Te₃ with a single Dirac cone on the surface. *Nature Physics* **5**, 438–442 (2009).
- [60] Chen, Y. *et al.* Experimental realization of a three-dimensional topological insulator, Bi₂Te₃. *Science* **325**, 178–181 (2009).
- [61] Matthias, B. T. Superconducting compounds of nonsuperconducting elements. *Phys. Rev.* **90**, 487–487 (1953).

- [62] Karki, A. B., Browne, D. A., Stadler, S., Li, J. & Jin, R. PdTe: a strongly coupled superconductor. *Journal of Physics: Condensed Matter* **24**, 055701 (2012).
- [63] *See Supplemental Materials for more details.*
- [64] Sharma, M., Sang, L., Rani, P., Wang, X. & Awana, V. Bulk superconductivity below 6 K in PdBi₂Te₃ topological single crystal. *Journal of Superconductivity and Novel Magnetism* **33**, 1243–1247 (2020).
- [65] Wang, X. *et al.* Identify the nematic superconductivity of topological superconductor Pd_xBi₂Te₃ by angle-dependent upper critical field measurement. *Journal of Superconductivity and Novel Magnetism* **34**, 3045–3052 (2021).
- [66] Fu, L., Kane, C. L. & Mele, E. J. Topological insulators in three dimensions. *Phys. Rev. Lett.* **98**, 106803 (2007).
- [67] Baroni, S., de Gironcoli, S., Dal Corso, A. & Giannozzi, P. Phonons and related crystal properties from density-functional perturbation theory. *Rev. Mod. Phys.* **73**, 515–562 (2001).
- [68] McMillan, W. L. Transition temperature of strong-coupled superconductors. *Phys. Rev.* **167**, 331–344 (1968).
- [69] Allen, P. B. & Dynes, R. C. Transition temperature of strong-coupled superconductors reanalyzed. *Phys. Rev. B* **12**, 905–922 (1975).
- [70] Kresse, G. & Hafner, J. Ab initio molecular dynamics for open-shell transition metals. *Physical Review B* **48**, 13115 (1993).
- [71] Kresse, G. & Furthmüller, J. Efficiency of ab-initio total energy calculations for metals and semiconductors using a plane-wave basis set. *Computational Materials Science* **6**, 15–50 (1996).
- [72] Perdew, J. P., Burke, K. & Ernzerhof, M. Generalized gradient approximation made simple. *Phys. Rev. Lett.* **77**, 3865–3868 (1996).
- [73] Klimeš, J. c. v., Bowler, D. R. & Michaelides, A. Van der waals density functionals applied to solids. *Phys. Rev. B* **83**, 195131 (2011).
- [74] Giannozzi, P. *et al.* Quantum espresso: a modular and open-source software project for quantum simulations of materials. *Journal of physics: Condensed Matter* **21**, 395502 (2009).
- [75] Togo, A. & Tanaka, I. First principles phonon calculations in materials science. *Scr. Mater.* **108**, 1–5 (2015).
- [76] Mostofi, A. A. *et al.* wannier90: A tool for obtaining maximally-localised wannier functions. *Computer Physics Communications* **178**, 685–699 (2008).

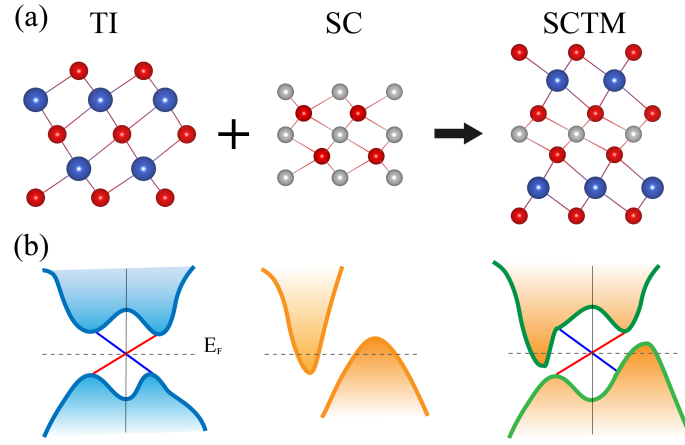


FIG. 1. The strategy to design idea SCTMs by intercalating the SC units into the TI.

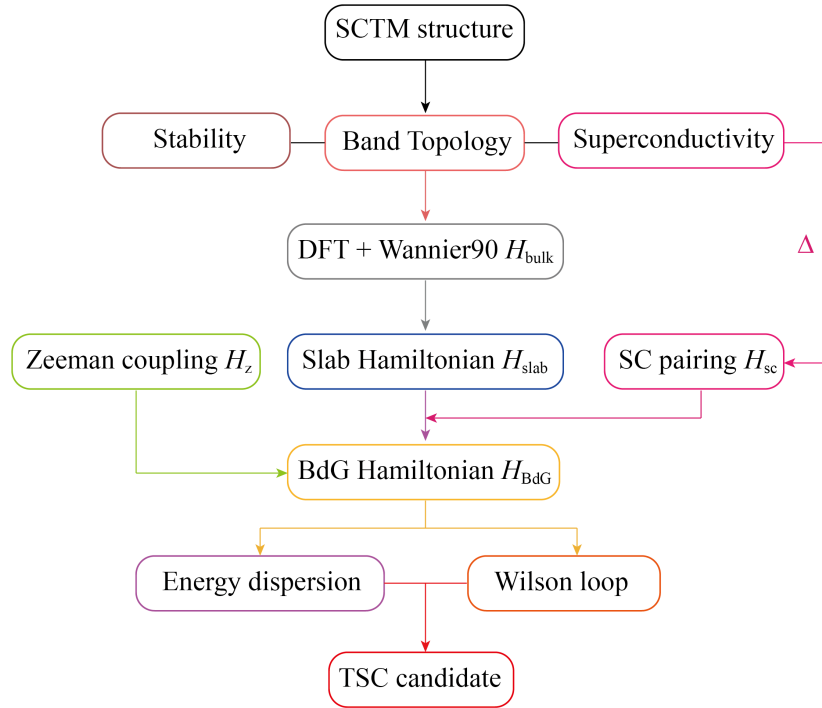


FIG. 2. The generic flow chart to characterize the TSC properties from ab initio calculations.

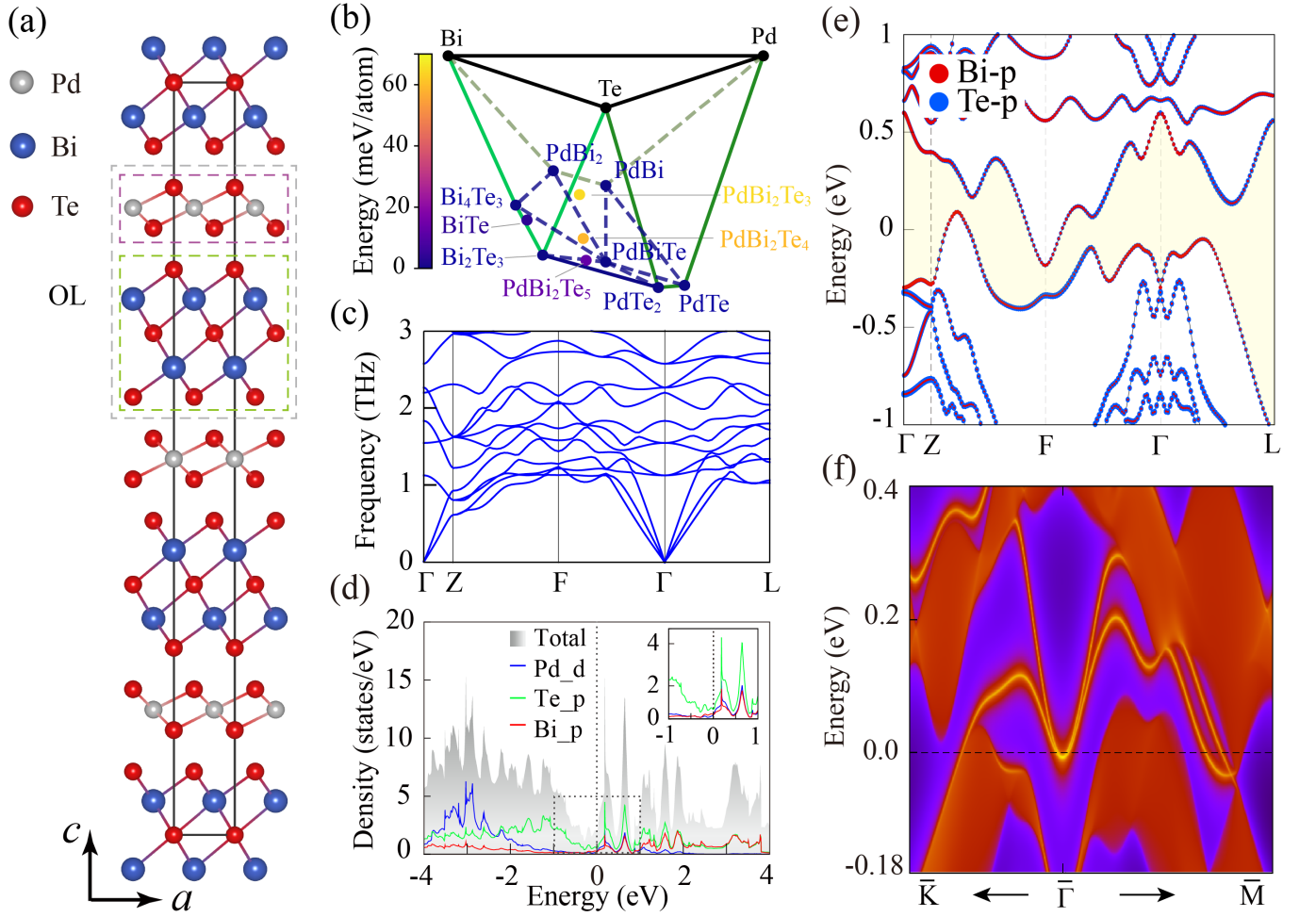


FIG. 3. (a) The side view of the crystal structures of PdBi_2Te_5 , in which the octuple-layer (OL) unit of PdBi_2Te_5 formed by the Bi_2Te_3 quintuple-layer and PdTe_2 triple-layer is marked by a grey dashed rectangle. (b) Convex hull diagram for Pd-Bi-Te system, the energy above convex hull is displayed by color-bar. (c) The phonon dispersion of PdBi_2Te_5 . (d) The total DOS and projected DOS of the Pd, Te, Bi atoms in PdBi_2Te_5 , the zoom-in image shows the projected DOS near the Fermi level. (e) The orbital-projected band structures of PdBi_2Te_5 , where a continuous band gap around the Fermi level is marked by the yellow shade. (f) The topological surface states on (001) surface of PdBi_2Te_5 .

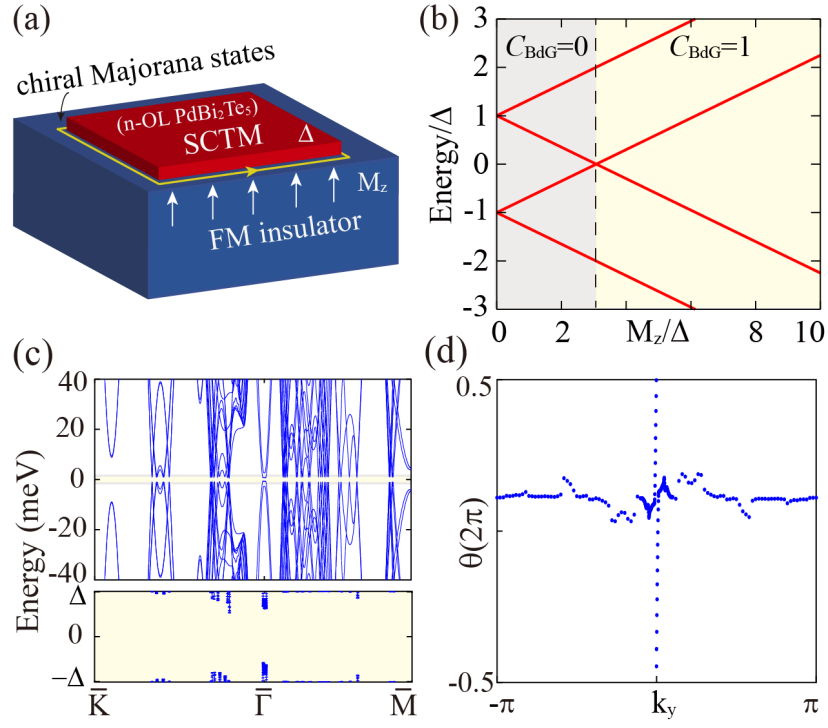


FIG. 4. (a) The schematic to realize chiral TSC in PdBi₂T₅ slab. (b) The low energy spectrum at the Γ point as the function of Zeeman splitting energy M_z . (c) The superconducting spectrum along high symmetry paths with $M_z = 5$ meV and $\Delta = 1$ meV, the zoom-in image shows the full gap in the whole BZ. (d) The Wilson loop spectrum for all occupied states of 4(c), which manifest the superconducting BdG Chern number $C_{\text{BdG}} = 1$ clearly.

Supplementary Material: Topological superconductor candidates PdBi_2Te_4 and PdBi_2Te_5 from a generic ab initio strategy

Aiyun Luo,^{1,*} Ying Li,^{1,*} Yi Qin,^{1,*} Jingnan Hu,¹ Biao Lian,² and Gang Xu^{1,3,4,†}

¹Wuhan National High Magnetic Field Center & School of Physics,
Huazhong University of Science and Technology, Wuhan 430074, China

²Department of Physics, Princeton University, Princeton, NJ 08544, United States of America

³Institute for Quantum Science and Engineering,
Huazhong University of Science and Technology, Wuhan 430074, China

⁴Wuhan Institute of Quantum Technology, Wuhan 430074, China

I. The crystal structures of PdBi_2Te_5 and PdBi_2Te_4

The crystal structures of PdBi_2Te_5 are shown in Fig. S1. Since both Bi_2Te_3 (Fig. S1(a)) and PdTe_2 (Fig. S1(b)) are Van der Waals materials, a naturally stable unit of PdBi_2Te_5 would be an octuple-layer (OL) block as shown in Fig. S1(e). With different stacking sequences along c -direction, the crystal structures of AA-stacking, AB-stacking and ABC-stacking are shown in Fig. S1(c), (d) and (e), respectively. As a result, the relaxed lattice parameters and total energies of these structures are tabulated in Table. S1. Our calculated results demonstrate that the most stable structure of PdBi_2Te_5 is the ABC-stacking rhombohedral unit cell as shown in Fig. S1(e), which is 73 meV/f.u. and 46 meV/f.u. lower than the AA and AB stacking structures.

The crystal structures of PdBi_2Te_4 are shown in Fig. S2, which is formed by the integration of Bi_2Te_3 (Fig. S2(a)) and PdTe (Fig. S2(b)). Like the construction of MnBi_2Te_4 [1, 2], a naturally stable unit of PdBi_2Te_4 would be a septuple-layer (SL) block as shown by the grey dash rectangle in Fig. S2(c)-(e). Similar to the case of PdBi_2Te_5 , the relaxed lattice parameters and total energies of AA-stacking, AB-stacking, and ABC-stacking sequences of PdBi_2Te_4 are tabulated in Table. S2. Our calculations demonstrate that SL- PdBi_2Te_4 favor the ABC stacking rhombohedral unit cell as shown in Fig. S2(e), which is 73 meV/f.u. and 12 meV/f.u. lower than the AA(Fig. S2(c)) and AB(Fig. S2(d)) stacking structures.

* These authors made equal contributions to this work.

† e-mail address: gangxu@hust.edu.cn

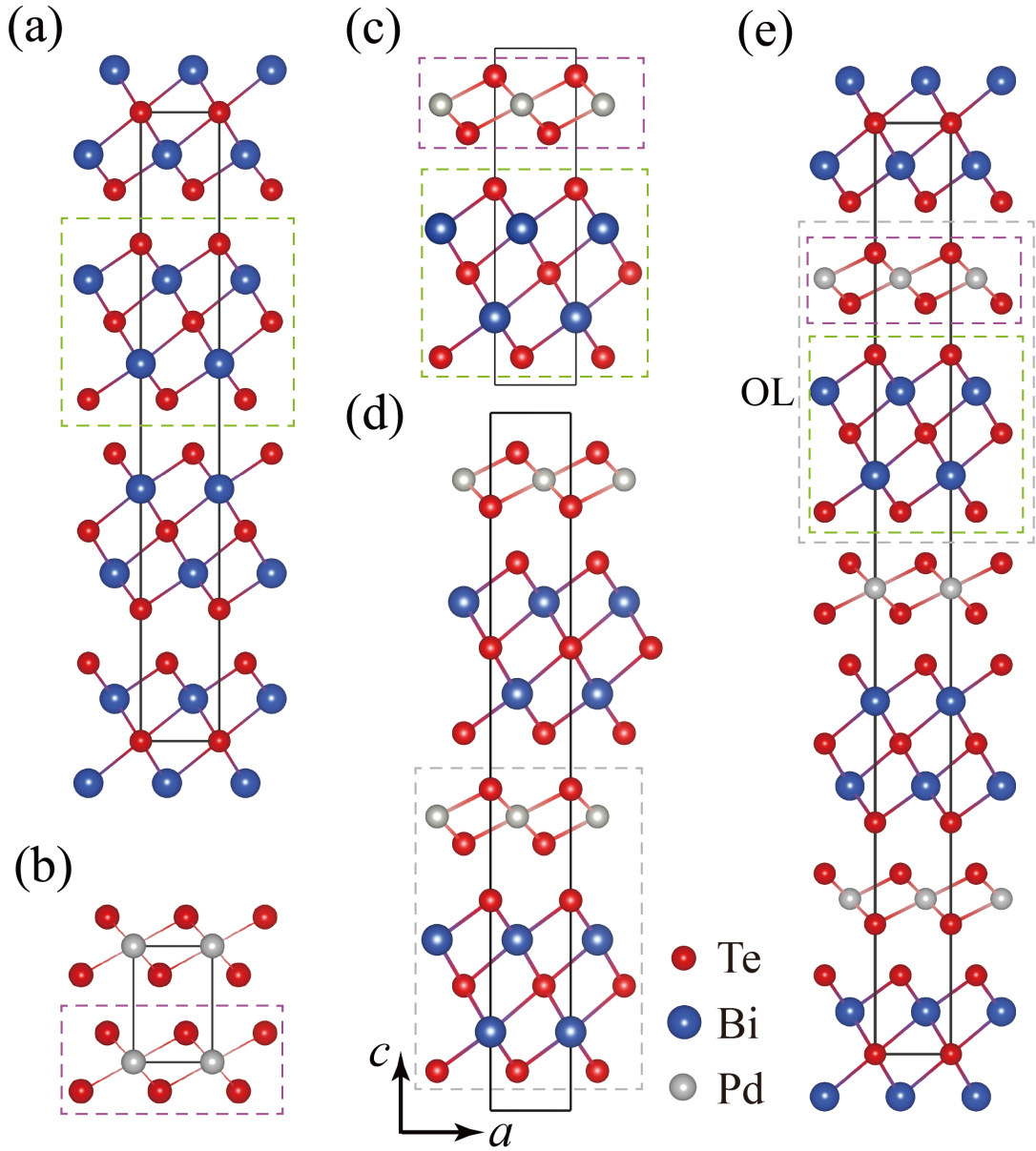


FIG. S1. The crystal structures of different stacking sequences of PdBi_2Te_5 . (a) A side view of the crystal structures of Bi_2Te_3 , the quintuple-layer block is marked by the green dashed rectangle. (b) PdTe_2 , the triple-layer block is marked by the purple dashed rectangle. PdBi_2Te_5 for (c) AA stacking, (d) AB stacking, and (e) ABC stacking, respectively. A octuple-layer (OL) block of PdBi_2Te_5 is marked by the grey dashed rectangle.

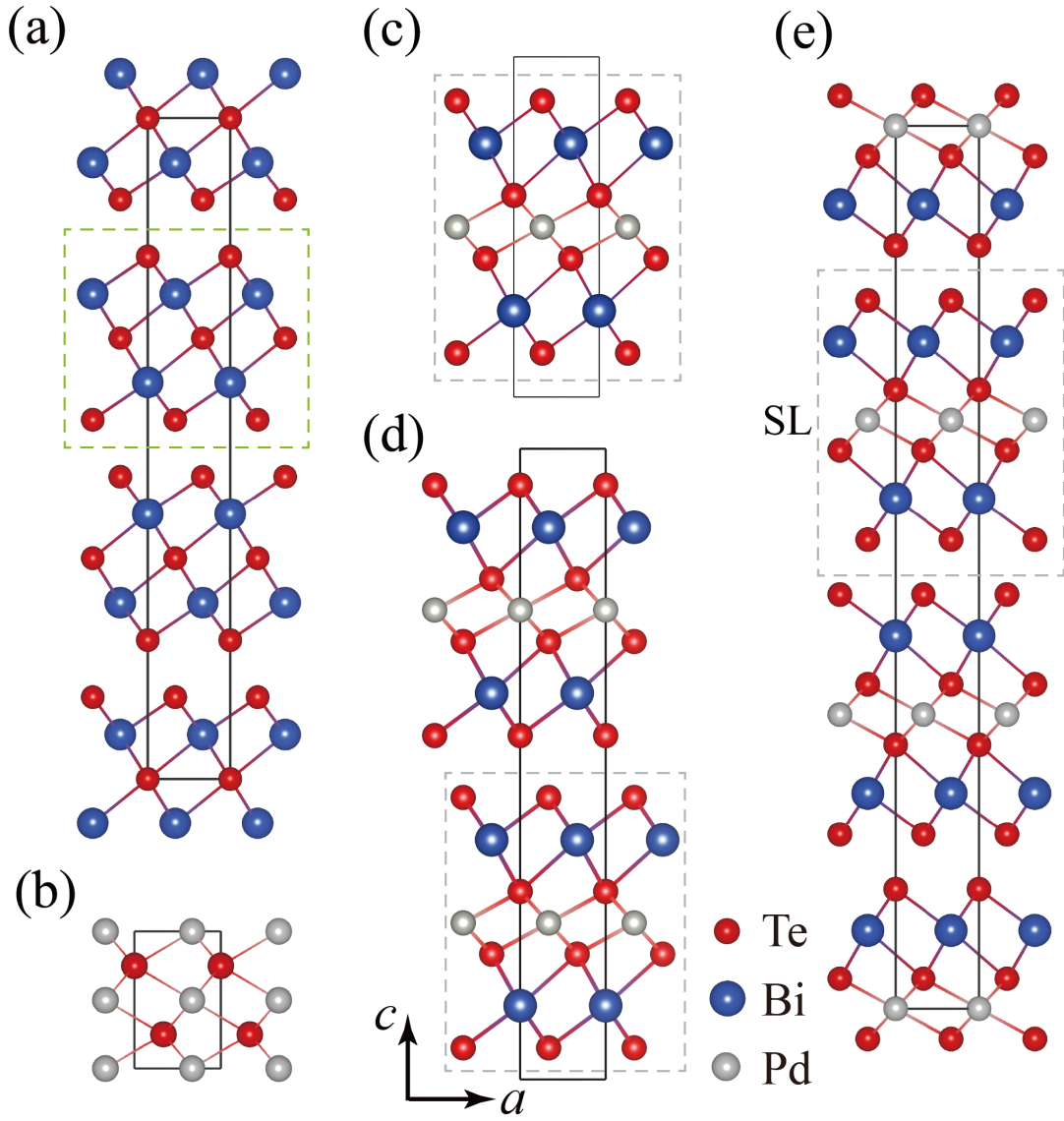


FIG. S2. The crystal structures of different stacking sequences of PdBi_2Te_4 . (a) Bi_2Te_3 . (b) PdTe . PdBi_2Te_4 for (c) AA stacking, (d) AB stacking, and (e) ABC stacking, respectively. A SL block of PdBi_2Te_4 is marked by the grey dashed rectangle.

TABLE S1. The crystal parameters and total energies of different stacking sequences of PdBi₂Te₅ from our relaxed results.

Compound	Stacking	Space group	Lattice (Å)	Atom	Wyckoff	Coordinate	Energy(eV/f.u.)
PdBi ₂ Te ₅	AA	<i>P3m1</i>	a = b = 4.287 c = 16.325	Pd	1c	(0.667, 0.333, 0.013)	-30.385
				Bi1	1a	0, 0, 0.363	
				Bi2	1a	0, 0, 0.623	
				Te1	1b	(0.333, 0.667, 0.090)	
				Te2	1b	(0.333, 0.667, 0.492)	
				Te3	1c	(0.667, 0.333, 0.251)	
				Te4	1c	(0.667, 0.333, 0.936)	
				Te5	1a	(0, 0, 0.733)	
PdBi ₂ Te ₅	AB	<i>P3m1</i>	a = b = 4.315 c = 30.987	Pd1	1c	(0.667, 0.333, 0.483)	-30.412
				Pd2	1a	(0, 0, 0)	
				Bi1	1b	(0.333, 0.667, 0.792)	
				Bi2	1c	(0.667, 0.333, 0.658)	
				Bi3	1c	(0.667, 0.333, 0.308)	
				Bi4	1a	(0, 0, 0.175)	
				Te1	1b	(0.333, 0.667, 0.046)	
				Te2	1b	(0.333, 0.667, 0.437)	
				Te3	1b	(0.333, 0.667, 0.600)	
				Te4	1b	(0.333, 0.667, 0.241)	
Te5	1c	(0.667, 0.333, 0.956)					
Te6	1c	(0.667, 0.333, 0.115)					
Te7	1c	(0.667, 0.333, 0.851)					
Te8	1a	(0, 0, 0.528)					
Te9	1a	(0, 0, 0.726)					
Te10	1a	(0, 0, 0.367)					
PdBi ₂ Te ₅	ABC	<i>R$\bar{3}m$</i>	a = b = 4.304 c = 46.391	Pd	3b	(0, 0, 0.5)	-30.458
				Bi	6c	(0, 0, 0.3788)	
				Te1	3a	(0, 0, 0)	
				Te2	6c	(0, 0, 0.1396)	
Te3	6c	(0, 0, 0.2488)					

TABLE S2. The crystal parameters and total energies of different stacking sequences of PdBi₂Te₄ from our relaxed results.

Compound	Stacking	Space group	Lattice (Å)	Atom	Wyckoff	Coordinate	Energy(eV/f.u.)
PdBi ₂ Te ₄	AA	$P\bar{3}m1$	a = b = 4.275 c = 13.035	Pd	1b	(0, 0, 0.5)	-26.776
				Bi	2d	(0.667, 0.333, 0.2325)	
				Te1	2d	(0.333, 0.667, 0.397)	
				Te2	2c	(0, 0, 0.09)	
PdBi ₂ Te ₄	AB	$P\bar{3}m1$	a = b = 4.275 c = 26.070	Pd	2d	(0.333, 0.667, 0.75025)	-26.837
				Bi1	2c	(0, 0, 0.61675)	
				Bi2	2d	(0.667, 0.333, 0.88375)	
				Te1	2d	(0.333, 0.667, 0.95375)	
				Te2	2d	(0.333, 0.667, 0.54675)	
				Te3	2c	(0, 0, 0.80175)	
Te4	2d	(0.667, 0.333, 0.88375)					
PdBi ₂ Te ₄	ABC	$R\bar{3}m$	a = b = 4.296 c = 40.546	Pd	3a	(0, 0, 0)	-26.849
				Bi	6c	(0, 0, 0.4215)	
				Te1	6c	(0, 0, 0.3000)	
				Te2	6c	(0, 0, 0.8668)	

II. The detailed crystal parameters and formation energies of Pd-Bi-Te compounds for convex hull

The fundamental thermodynamic nature of Pd-Bi-Te compounds can be fully characterized in terms of the convex hull diagram [3, 4], which is defined as formation energy *versus* composition diagram with the ground state at special compositions. For all of the known Pd-Bi-Te compounds as tabulated in Table. S3, we calculate their formation energy and tabular the results in Table. S4. Based on these results, we construct the convex hull diagram of Pd-Bi-Te compounds in Fig.3(b) of the main text. The ternary compounds PdBi_2Te_3 , PdBi_2Te_4 and Pd_2Te_5 are 65 meV/atom, 59 meV/atom and 13 meV/atom above the convex hull respectively, indicating that they are metastable phases with respect to decomposition into the energetically favorable binary phases. Significantly, PdBi_2Te_3 above the convex hull has already been synthesized in experiments, which is higher 52 meV/atom and 7 meV/atom than PdBi_2Te_5 and PdBi_2Te_4 . Therefore, we expect that PdBi_2Te_5 and PdBi_2Te_4 could be synthesized in the future.

TABLE S3. The space group, lattice constants and atomic coordinates of Pd-Bi-Te compounds used in the convex hull.

Compound	Space group	Lattice (Å)	Atom	Wyckoff	Coordinate
Pd	$Fm\bar{3}m$	a = b = c = 3.889	Pd	4a	(0, 0, 0)
Bi	$R\bar{3}m$	a = 4.523, c = 11.800	Bi	3b	(0, 0, 0.227)
Te	$P3_121$	a = 4.445, c = 5.91	Te	3a	(0.225, 0.0, 0.0)
PdBi	$Cmc2_1$	a = 8.707 b = 7.203 c = 10.662	Pd1	8b	(0.274, 0.125, 0.053)
			Pd2	4a	(0, 0.108, 0.225)
			Pd3	4a	(0, 0.65, 0.225)
			Bi1	8b	(0.226, 0.375, 0.278)
			Bi2	4a	(0, 0.108, 0.5)
			Bi3	4a	(0, 0.35, 0)
PdBi ₂	$I4/mmm$	a = b = 3.362 c = 12.983	Pd	2a	(0, 0, 0)
			Bi	4e	(0, 0, 0.363)
PdTe	$P6_3/mmc$	a = b = 4.152 c = 5.671	Pd	2a	(0, 0, 0)
			Te	2c	(0.333, 0.667, 0.25)
PdTe ₂	$P\bar{3}m1$	a = b = 4.028 c = 5.118	Pd	1a	(0, 0, 0)
			Te	2d	(0.333, 0.667, 0.25)
BiTe	$P\bar{3}m1$	a = b = 4.400 c = 24.000	Bi1	2d	(0.333, 0.667, 0.291)
			Bi2	2d	(0.333, 0.667, 0.541)
			Bi3	2c	(0, 0, 0.126)
			Te1	2d	(0.333, 0.667, 0.056)
			Te2	2d	(0.333, 0.667, 0.789)
			Te3	2c	(0, 0, 0.362)
Bi ₂ Te ₃	$R\bar{3}m$	a = b = 4.35 c = 30.36	Bi	6c	(0, 0, 0.600)
			Te1	6c	(0, 0, 0.790)
			Te2	3a	(0, 0, 0)
Bi ₄ Te ₃	$R\bar{3}m$	a = b = 4.451 c = 41.888	Bi1	6c	(0, 0, 0.146)
			Bi2	6c	(0, 0, 0.283)
			Te1	6c	(0, 0, 0.426)
			Te2	3a	(0, 0, 0)
PdBi ₂ Te ₃	$R\bar{3}m$	a = b = 4.421 c = 30.337	Pd	3b	(0, 0, 0.5)
			Bi	6c	(0, 0, 0.561)
			Te1	3a	(0, 0, 0)
			Te2	6c	(0, 0, 0.796)

TABLE S4. The total energy and formation energy of Pd-Bi-Te compounds used in the convex hull.

Compound	Energy(eV/f.u.)	Formation energy(eV/atom)
Pd	-5.161	–
Bi	-3.804	–
Te	-2.901	–
PdTe	-9.022	-0.480
PdTe ₂	-1.349	-0.450
PdBi	-9.565	-0.3
PdBi ₂	-13.568	-0.266
BiTe	-7.346	-0.320
Bi ₂ Te ₃	-18.258	-0.389
Bi ₄ Te ₃	-25.979	-0.294
PdBi ₂ Te ₃	-23.038	-0.261
PdBi ₂ Te ₄	-26.849	-0.354
PdBi ₂ Te ₅	-30.458	-0.398

III. The phonon spectrum, electronic structures and superconducting properties of PdBi₂Te₄

In Fig. S3(a), we calculate and plot the phonon dispersion of PdBi₂Te₄. It clearly shows that there are 21 phonon modes with fully real positive frequencies, indicating that the rhombohedral PdBi₂Te₄ are dynamically stable. Based on the stable rhombohedral structure, we carry out the calculations with SOC of electronic properties of PdBi₂Te₄. The total and projected density of states (DOS) are shown in Fig. S3(b), which shows that the total DOS at the Fermi level is about of 3.95 states/eV, indicating its metallic nature and the probability of superconductivity. Fig. S3(c) shows the projected band structures of PdBi₂Te₄, from which we can see that two bands with *p*-orbital components from Te or Bi cross the Fermi level and a continuous direct gap (the yellow region in Fig. S3(c)) exists around the Fermi level. Further detailed orbital components analysis demonstrates that band inversion is present between the nominal valence band and conduction band, indicating the non-trivial band topology of bulk PdBi₂Te₄. In Fig. S3(d), we calculate and plot the topological surface states on the (001) surface of PdBi₂Te₄, in which the Dirac surface states at the Γ point manifest approximately -62 meV below the Fermi level, confirming PdBi₂Te₄ is a Z_2 topological metal.

To investigate the superconducting properties of PdBi₂Te₄ and PdBi₂Te₅, we calculate their electron-phonon coupling constant λ and logarithmic average phonon frequency ω_{\log} as tabulated in Table. S5. As a comparison, the λ and ω_{\log} of parent SC PdTe and PdTe₂ are also calculated. Moreover, the superconducting transition temperature (T_c) is estimated by using the reduced Allen-Dynes formula as Eq.(4) in the main text. By adopting a typical $\mu^* = 0.1$, the T_c of PdBi₂Te₄ and PdBi₂Te₅ is estimated as 3.11 K and 0.57 K, respectively. Furthermore, the T_c of PdTe and PdTe₂ is estimated as 2.55 K and 1.59 K, which are consistent with the experimental results very well [5–9]. These results clearly demonstrate that the SC in PdTe and PdTe₂ is well inherited into the bulk of PdBi₂Te₄ and PdBi₂Te₅.

TABLE S5. The calculated electron-phonon coupling strength λ , logarithmic average phonon frequency ω_{\log} and the estimated T_c ($\mu^* = 0.1$) of PdTe, PdTe₂, PdBi₂Te₄ and PdBi₂Te₅.

Compound	λ	$\omega_{\log}(\text{cm}^{-1})$	$T_c(\text{K})$	$T_c^{exp}(\text{K})$
PdTe	0.61	106	2.55	2.3 [5], 4.5 [6]
PdTe ₂	0.52	112	1.59	1.64 [7–9]
PdBi ₂ Te ₄	0.70	89	3.11	–
PdBi ₂ Te ₅	0.43	97	0.57	–

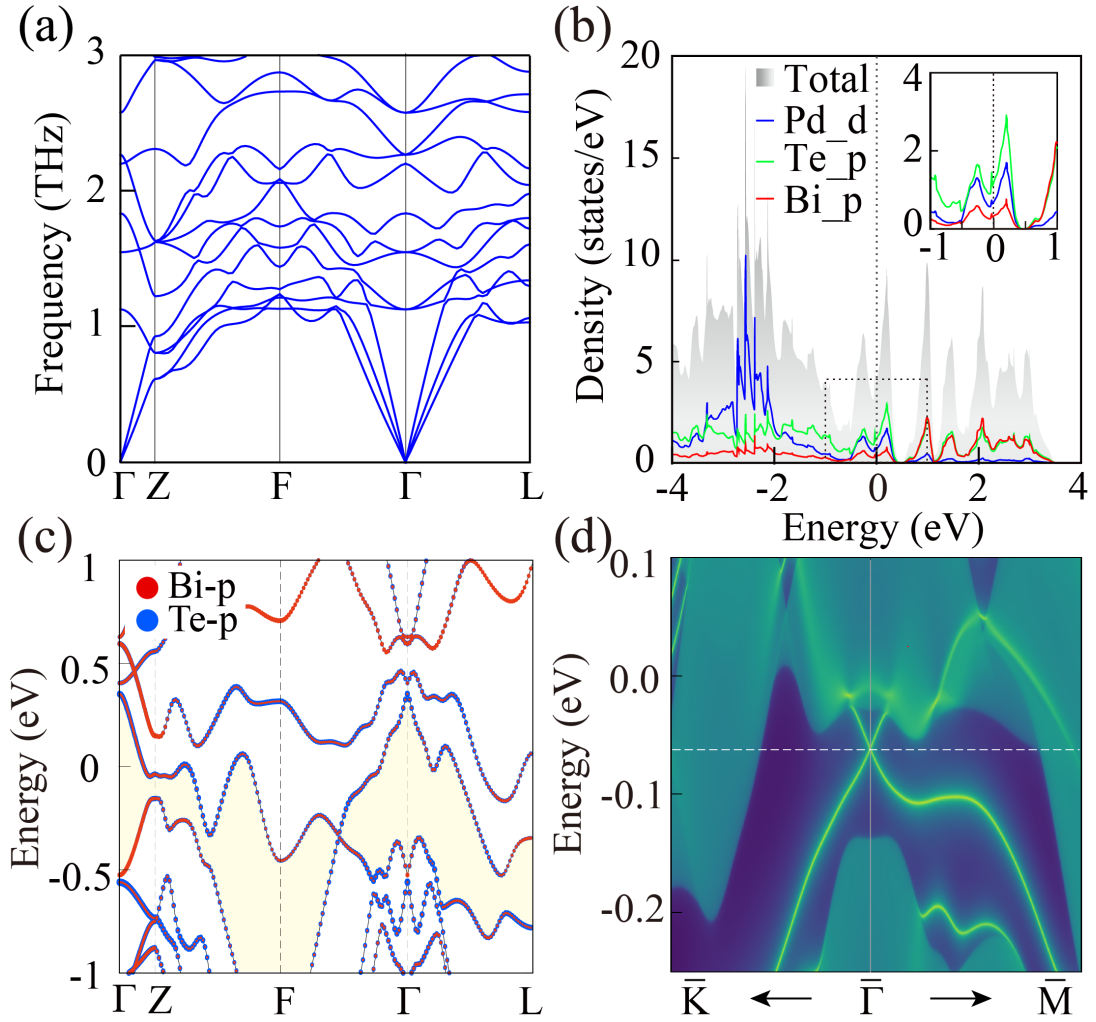


FIG. S3. The phonon dispersion and electronic properties of PdBi_2Te_4 . (a) The phonon dispersion of PdBi_2Te_4 . (b) The total DOS and projected DOS of the Pd, Te, Bi atoms in PdBi_2Te_4 , the zoom-in image shows the projected DOS near the Fermi level. (c) The orbital-projected band structures of PdBi_2Te_4 , a continuous band gap around the Fermi level is marked by the yellow shade. (d) The topological surface states on (001) surface of PdBi_2Te_4 .

IV. The chiral TSC phase in PdBi_2Te_4

In this section, we study the chiral TSC phase in 20-SL PdBi_2Te_4 by incorporating its topological and superconducting properties with Zeeman splitting. In this case, the chemical potential μ is set at the energy of surface Dirac cone at the Γ point (about -62 meV below the Fermi level), the estimated s -wave superconducting gap $\Delta_s = 1.0$ meV is introduced globally for all 20-SLs, and the out-of-plane Zeeman splitting is applied only in the bottom layer. In Fig. S4(a), we show the low energy spectrum of H_{BdG} at Γ point as a function of Zeeman splitting energy M_z , which manifests that two superconducting bands cross each other at critical point $M_z/\Delta = 5$. This behavior indicates that

a topological phase transition happens at the critical point. Fig. S4(b) shows the superconducting energy dispersion with $M_z=10$ meV and $\Delta=1$ meV. Its zoomed-in image, calculated in the whole BZ, directly reveals the full gap characters of superconducting spectrum, indicating that the system is a well defined chiral TSC. To further verify its nontrivial topological properties, the superconducting BdG Chern number for all occupied states is calculated by the Wilson loop method as shown in Fig. S4(c). The spectrum of Wilson loop exhibits a non-trivial chiral winding number 1, which directly confirms the superconducting BdG Chern number $C_{\text{BdG}} = 1$.

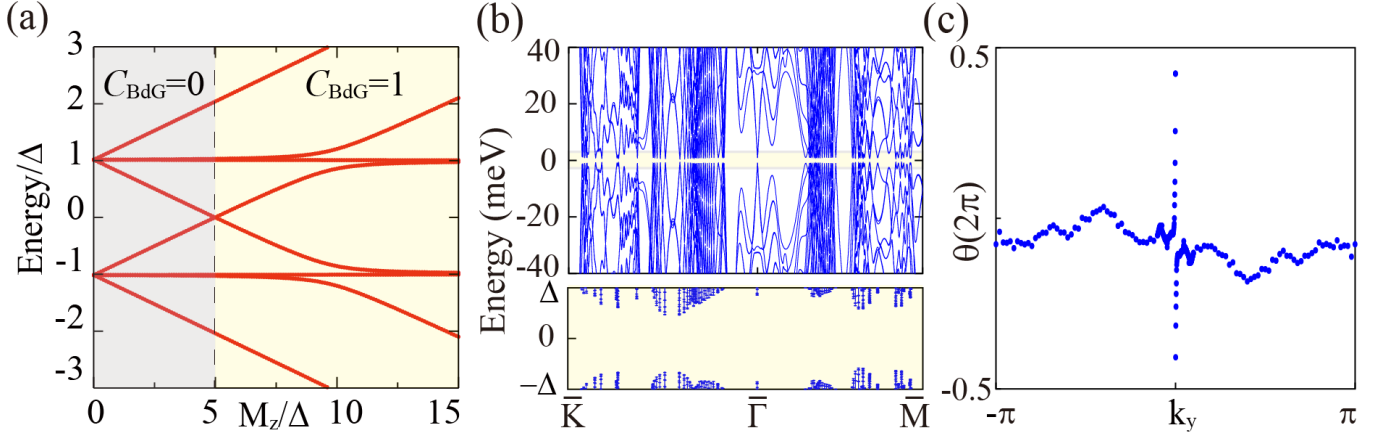


FIG. S4. The chiral TSC phase in slab PdBi₂T₄. (a) The low energy spectrum at the Γ point as the function of Zeeman splitting energy M_z , where $\Delta = 1$ meV. (b) The superconducting spectrum along high symmetry paths with $M_z = 10$ meV and $\Delta = 1$ meV, the zoom-in image shows the full gap in the whole BZ. (c) The Wilson loop spectrum of all occupied states in (b), which manifest the superconducting BdG Chern number $C_{\text{BdG}} = 1$ clearly.

V. The electronic structures and topological properties of AuBi₂Te₅

The crystal structure of rhombohedral AuBi₂Te₅ is shown in Fig. S5(a), which is formed by the layered intercalation of Bi₂Te₃ and AuTe₂. In Fig. S5(b), we show the calculated phonon dispersion along the high symmetry lines of AuBi₂Te₅, in which the most important observation is that all phonon modes have positive frequency throughout the BZ, indicating the dynamical stability of the rhombohedral structure. In Fig. S5(c), we calculate and plot the total and projected DOS of AuBi₂Te₅, which gives rise to $\text{DOS}(0 \text{ eV})=5.41$ states/eV at Fermi level, indicating its metallic nature and the possibility of superconductivity. Fig. S5(d) shows the orbital-projected band structures of AuBi₂Te₅, in which a continuous band gap around the Fermi level is marked by the yellow shades. Further detailed orbital components analysis demonstrates that a band inversion exists between the nominal valence band and conduction

band, which implies that AuBi_2Te_5 is a topological metal that inherits from parent Bi_2Te_3 . In Fig. S5(e), we show the calculated surface states of AuBi_2Te_5 in the (001) surface. It clearly shows that the topological surface states are presented in the bulk gap, confirming AuBi_2Te_5 is a Z_2 topological metal.

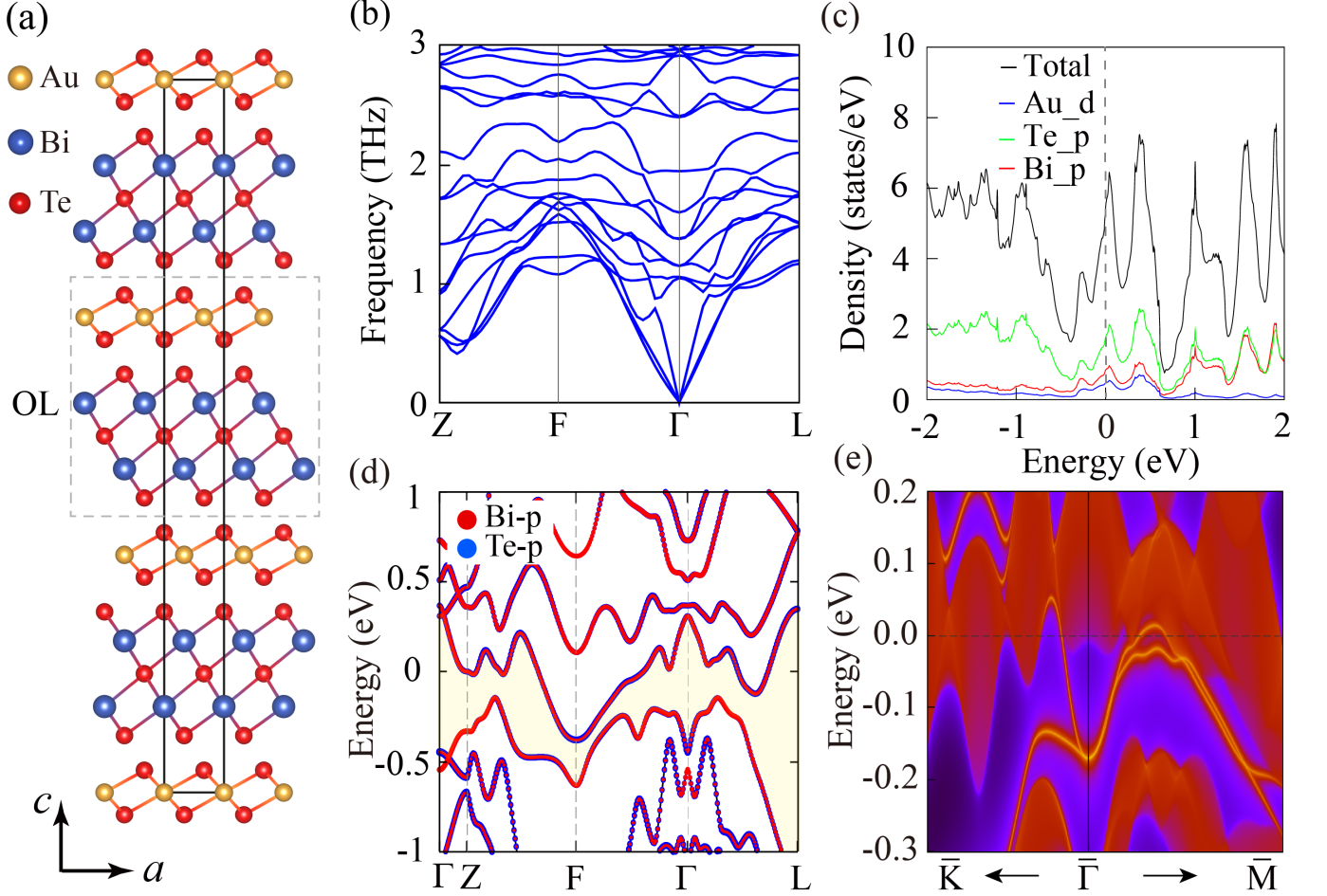


FIG. S5. The crystal structure, phonon dispersion, and electronic properties of AuBi_2Te_5 . (a) The side view of the crystal structure. (b) The phonon dispersion along high symmetry path. (d) The total DOS and projected DOS of the Au, Te, Bi atoms. (e) The orbital-projected band structures, a continuous band gap around the Fermi level is marked by the yellow shade. (f) The topological surface states on (001) surface.

-
- [1] Lee, D. S. *et al.* Crystal structure, properties and nanostructuring of a new layered chalcogenide semiconductor, Bi_2MnTe_4 . *CrystEngComm* **15**, 5532–5538 (2013).
- [2] Zhang, D. *et al.* Topological axion states in the magnetic insulator MnBi_2Te_4 with the quantized magnetoelectric effect. *Phys. Rev. Lett.* **122**, 206401 (2019).

- [3] Sun, Y., Lv, J., Xie, Y., Liu, H. & Ma, Y. Route to a superconducting phase above room temperature in electron-doped hydride compounds under high pressure. *Phys. Rev. Lett.* **123**, 097001 (2019).
- [4] Sharan, A. & Lany, S. Computational discovery of stable and metastable ternary oxynitrides. *The Journal of Chemical Physics* **154**, 234706 (2021).
- [5] Matthias, B. T. Superconducting compounds of nonsuperconducting elements. *Phys. Rev.* **90**, 487–487 (1953).
- [6] Karki, A. B., Browne, D. A., Stadler, S., Li, J. & Jin, R. PdTe: a strongly coupled superconductor. *Journal of Physics: Condensed Matter* **24**, 055701 (2012).
- [7] Kudo, K., Ishii, H. & Nohara, M. Composition-induced structural instability and strong-coupling superconductivity in $\text{Au}_{1-x}\text{Pd}_x\text{Te}_2$. *Phys. Rev. B* **93**, 140505 (2016).
- [8] Leng, H., Paulsen, C., Huang, Y. K. & de Visser, A. Type-I superconductivity in the Dirac semimetal PdTe₂. *Phys. Rev. B* **96**, 220506 (2017).
- [9] Das, S. *et al.* Conventional superconductivity in the type-II Dirac semimetal PdTe₂. *Phys. Rev. B* **97**, 014523 (2018).